

Dissolution of Intermetallic Second-Phase Particles in Zircaloy-2 in High-Temperature Steam



WEICHENG ZHONG, XIANG LIU, PETER A. MOUCHE, JUN-LI LIN, DONGHEE PARK, MOHAMED S. ELBAKHSHWAN, SIMERJEET K. GILL, YANG REN, JAMES F. STUBBINS, and BRENT J. HEUSER

The stability of intermetallic second-phase particles (SPPs) in coated Zircaloy-2 was studied in 700 °C steam environments up to 20 hours. Hydrogen generated from high-temperature steam oxidation of uncoated Zr-induced δ -hydrides formation in the Zircaloy matrix. Synchrotron XRD demonstrated that longer exposure times increased hydride peak intensity and decreased intermetallic SPPs' peak intensity. Cross-sectional SEM analysis verified the intermetallic SPPs' volume fraction reduction. The size distribution of intermetallic SPPs was characterized and larger particles were dissolved at longer oxidation time. A correlation between the hydrogen concentration and the volume fraction of intermetallic SPPs at 700 °C steam environment was found, with the volume fraction of SPPs decreasing as hydrogen concentration increases.

<https://doi.org/10.1007/s11661-018-5090-5>

© The Minerals, Metals & Materials Society and ASM International 2019

I. INTRODUCTION

ZIRCONIUM-BASED alloys have been used in commercial light water nuclear reactors for decades due to their good corrosion resistance, strength and their low thermal neutron absorption. Transition elements, such as Sn, Ni, Fe, and Cr, are added in Zirconium-based alloys to improve the corrosion resistance and mechanical properties.^[1] Nickel, Fe and Cr have limited solubility in α -Zr, on the order of 100 weight parts per million (wppm) at room temperature.^[2] These elements are primarily found in Zircaloy as intermetallic second-phase particles (SPPs). Zircaloy-2 typically contains two types of SPPs, body-centered tetragonal $Zr_2(Fe,Ni)$ and hexagonal $Zr(Fe,Cr)_2$.^[3,4]

The influences of size, distribution, and morphology of intermetallic SPPs on the hydrogen uptake and corrosion have been studied previously.^[2,5-7] Intermetallic SPPs affect the hydrogen uptake by changing zirconia microstructure^[8] or by providing a fast route for hydrogen transport through metallic SPPs in Zr

oxide.^[6,9] Zircaloy with coarser SPPs' distribution absorbs a higher fraction of hydrogen during corrosion.^[6,10] Corrosion behavior of Zircaloy was also affected by the SPPs' size distribution. Zircaloy with finer and denser distribution of SPPs showed better corrosion resistance under operational conditions^[2,5] and in high-temperature steam environment.^[7] Supersaturation of Fe, Cr, and Ni in Zircaloy also affects the corrosion. Higher solute content in the matrix leads to higher nodular corrosion resistance.^[2] This is attributed to the aliovalent substitution of Zr in monoclinic zirconia.^[11,12]

Dissolution and amorphization of SPPs were observed in Zircaloy cladding after service in nuclear reactors.^[9,13,14] Irradiation is known to affect the microstructure and stoichiometry of intermetallic SPPs and to alter the supersaturation of alloying elements in Zr matrix.^[12] Amorphization of intermetallic SPPs by irradiation is attributed to the accumulated defects in the crystalline structure.^[14] Dissolution of SPPs was caused by displacement cascade damage associated with neutron irradiation,^[15] with a depletion of Fe observed in the outer shells of SPPs.^[14] The dissolution of SPPs leads to higher supersaturation of alloying elements in Zr matrix, which in turn affected the oxidation behavior.^[7,12]

Hydrogen is generated from the Zr oxidation in aqueous or steam environment, and hydrogen uptake induces hydride formation in the Zircaloy matrix. The question can then be raised regarding the hydrogen effect on the stability of SPPs. To our best knowledge, intermetallic SPPs' stability in high-temperature steam environments has not been discussed in published

WEICHENG ZHONG, XIANG LIU, PETER A. MOUCHE, JUN-LI LIN, DONGHEE PARK, JAMES F. STUBBINS, and BRENT J. HEUSER are with the Department of Nuclear, Plasma, and Radiological Engineering, University of Illinois, Urbana, IL 61801. Contact e-mail: bheuser@illinois.edu MOHAMED S. ELBAKHSHWAN is with the Department of Engineering Physics, University of Wisconsin-Madison, Madison, WI 53706. SIMERJEET K. GILL is with the Nuclear Science and Technology Department, Brookhaven National Laboratory, Upton, NY, 11973. YANG REN is with the X-ray Science Division, Argonne National Laboratory, Argonne, IL 60439.

Manuscript submitted August 15, 2018.

Article published online January 10, 2019

literature. The objective of this study is to study the dissolution of SPPs due to the hydrogen presence from the oxidation of the Zircaloy in high-temperature steam. In this study, we present the observation of SPPs' dissolution in Zircaloy-2 in high-temperature steam environment. This study is part of the oxidation response study of the coated Zircaloy to improve the oxidation resistance in high-temperature steam environment under the scope of Accident Tolerant Fuel.^[16,17] Chromium-Aluminum alloy coatings were deposited on Zircaloy-2 coupons, as shown in Figure 1(a). The coatings acted as protective barriers,^[16] preventing oxidation on the broad sides when the coupons were exposed to 700 °C steam. Hydrogen generated from the oxidation of the four uncoated edges was absorbed. Once the hydrogen concentration in matrix reached the terminal solid solubility, zirconium hydrides formed in the matrix. This coating geometry was beneficial for characterization of SPPs by synchrotron X-ray diffraction in transmission geometry. The coatings prevented Zr oxide phase formation, whose peaks could otherwise overlay with the peaks of SPPs. Therefore, the deposited coatings made SPPs' characterization by synchrotron XRD possible.

II. EXPERIMENTAL METHODS

A. Sample Preparations

Chromium-Aluminum coatings with the atomic composition of 81 pct Cr and 19 pct Al were deposited on Zircaloy-2 coupons *via* magnetron sputtering.^[17,18] Zircaloy-2 has a nominal composition (weight percent) of 1.5 pct Sn-0.15 pct Fe-0.1 pct Cr-0.05 pct Ni. Coatings were deposited as oxidation barriers for Zircaloy-2 substrate in elevated temperature.^[16] Coated Zircaloy-2

coupons were exposed to 700 °C steam for 1, 3, 5, 10, and 20 hours in a Netzsch Simultaneous Thermal Analysis (STA).^[17] Different exposure times at 700 °C were performed to obtain different hydrogen concentrations. Table I shows the sample matrix that includes coating parameters and coupon dimensions. To characterize intermetallic SPPs and zirconium hydrides using scanning electron microscopy (SEM), cross sections of coated Zircaloy were cut and polished, with 0.05 μm silica solution as a final polishing step. They were chemically etched using a solution of hydrofluoric acid, nitric acid, and distilled water in volume ratios of 5, 45, and 50 pct, respectively.

B. Analytical Techniques

The as-deposited pre- and post-exposure coated Zircaloy-2 were characterized using SEM, transmission electron microscopy (TEM), and synchrotron X-ray diffraction (XRD). Cross-sectional microstructures of the as-deposited and the post-exposure samples were studied by SEM for hydride distribution and the size distribution of intermetallic SPPs. A HITACHI S-4800 high-resolution SEM was used in this study. The electron source was a cold field emission gun, with 1-nm resolution at 15 kV. Focused Ion Beam (FIB) was used to prepare TEM samples at the center of the sample, which was cut through the cross section for the FIB lift-out, as shown in Figure 1(b). TEM was applied to observe the microstructures of hydride and intermetallic SPPs. A JEOL 2010LaB6 TEM operates at 200 kV and has the point resolution of 0.28 nm. Synchrotron XRD was applied to identify the sample crystal structure and to estimate the volume fraction of different phases. Synchrotron X-ray diffraction was performed at the Advanced Photon Source in

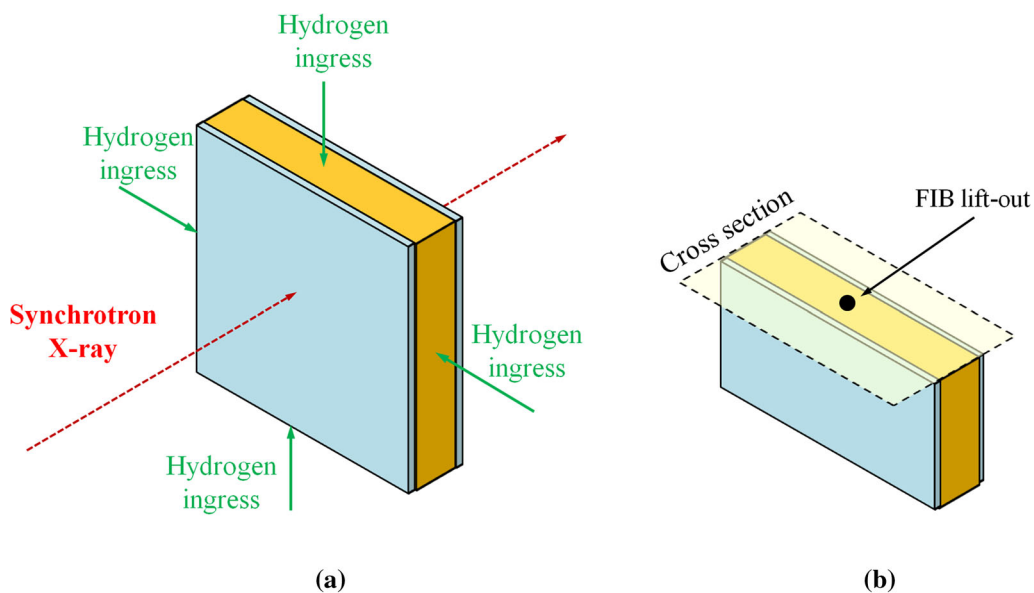


Fig. 1—Schematics of a CrAl-coated Zircaloy-2 coupon. (a) Coatings were deposited on two broad sides to prevent Zr oxidation. Hydrogen ingress from the edges due to the oxidation of uncoated edge. Synchrotron XRD was performed on the center of the broad side. (b) Cross section was made at sample mid-plane and FIB lift-out was performed at the center of the cross section.

Table I. Sample Matrix with Coatings Parameters and Samples Dimension

Sample ID	Coating Composition [Cr/Al in Atomic Percentage]	Coating Thickness (μm)	Exposure Time [h]	Sample Dimension [mm \times mm \times mm]
CrAl-0hr	81/19	1	0	10 \times 10 \times 1
CrAl-1hr	81/19	1	1	5 \times 5 \times 1
CrAl-3hr	81/19	1	3	5 \times 5 \times 1
CrAl-5hr	81/19	1	5	5 \times 5 \times 1
CrAl-10hr	81/19	1	10	5 \times 5 \times 1
CrAl-20hr	81/19	1	20	10 \times 10 \times 1

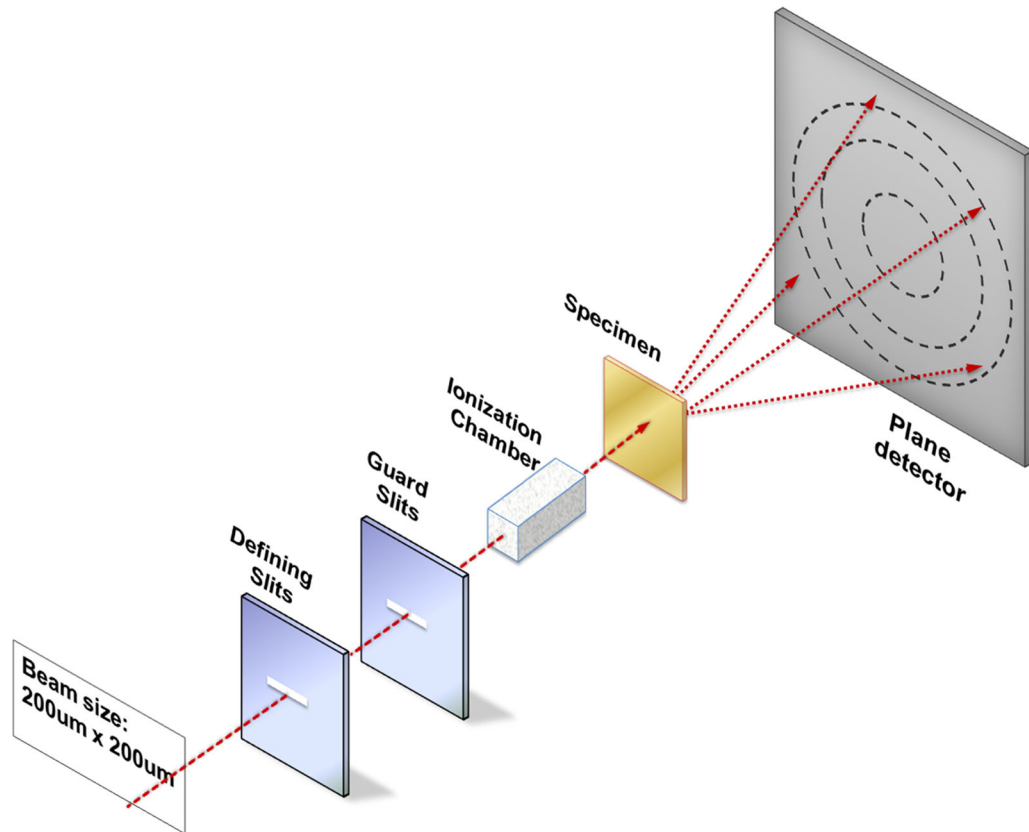


Fig. 2—Synchrotron X-ray setup in Sector 11ID-C in advanced photon source. X-ray energy is 105.6 keV. Sample–detector distance is 2.3 m. By this setup, lattice planes with the d spacing above 1.3 Å can be observed.

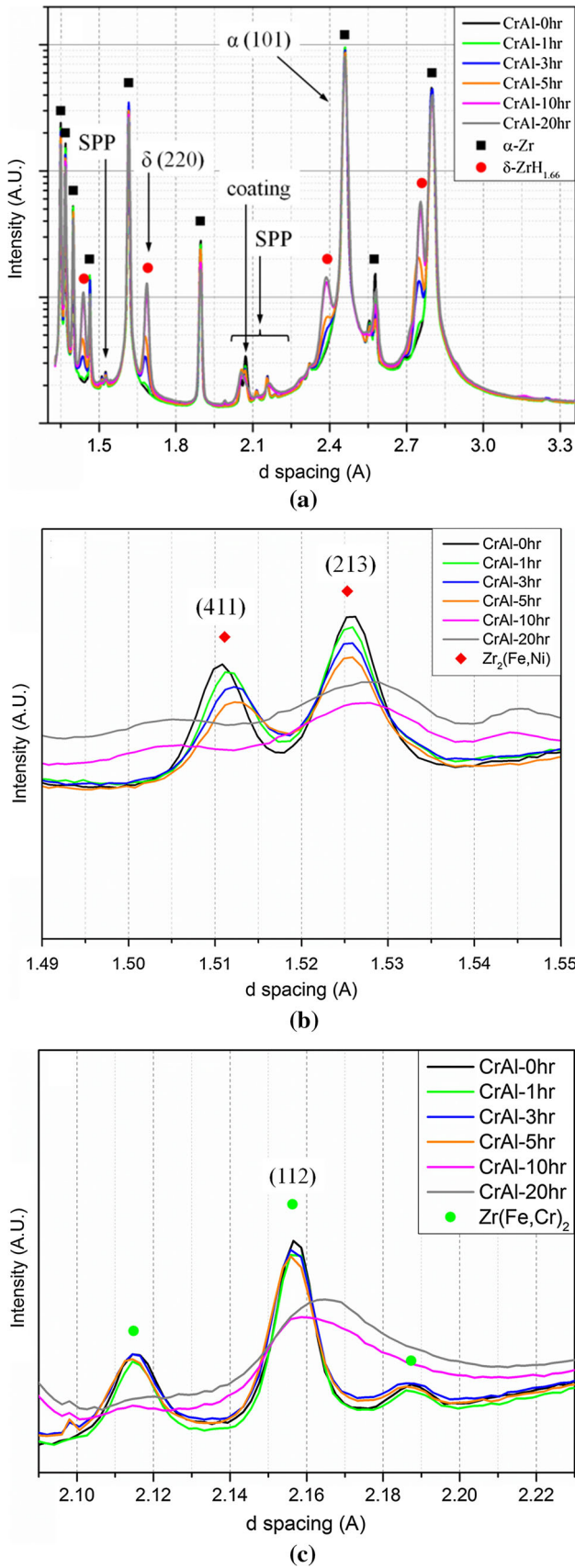
Section 11ID-C at Argonne National Laboratory. Figure 2 shows the schematics of the synchrotron X-ray setup. X-ray diffraction was performed on the center of coated side of the coupons in transmission geometry. The energy of the incident X-ray was 105.6 keV, which corresponded to a wavelength of 0.117 Å. Beam size was set to 200 μm by 200 μm . An area detector with the size of 1 m by 1 m was used. Distance between the samples and the detector was set at 2.3 m. In this geometry lattice planes with the d spacing above 1.3 Å could be observed. The total volume fraction of intermetallic SPPs in typical nuclear grade Zircaloy is of small percent,^[8] and typical bench-top X-ray diffraction does not have sufficient intensity and resolution to measure the SPPs in such low volume fraction.

III. RESULTS

A. Hydrogen Concentration Estimation

Hydride volume fraction and hydrogen concentration were estimated from the diffraction peak intensity of different phases. Figure 3 shows the synchrotron diffraction patterns of CrAl-coated coupons at different exposure times up to 20 hours. Zirconium hydride diffraction peaks were observed in the spectrum and indexed as the δ -ZrH_{1.66} phase (Fm-3m). The intensity from δ -hydride increased with the exposure time. Hydride volume was estimated using the following equation^[19]:

$$\frac{I_{\delta(220)}}{I_{\alpha(101)}} = \frac{R_{\delta(220)}}{R_{\alpha(101)}} \times \frac{V_{\delta}}{V_{\alpha}}, \quad [1]$$



◀ Fig. 3—Diffraction patterns of CrAl-coated Zircaloy at different exposure times. (a) Full spectrum from 1.3 to 3.3 Å. (b) Diffraction patterns from 1.49 to 1.55 Å showing peaks from Zr₂(Fe,Ni). (c) Diffraction patterns from 2.09 to 2.23 Å showing peaks from Zr(Fe,Cr)₂.

where $I_{\delta(hkl)}$ and $I_{\alpha(hkl)}$ are the integrated intensities of δ -hydride and α -Zirconium hkl peaks, respectively; V_{δ} , V_{α} are the volumes of δ -hydride and α -Zirconium phase; and R_{hkl} is a factor to relate the volume of a phase to the intensity. The Zr (101) peak and hydride (220) peak were selected for the volume calculation, as these two peaks were strong and not overlapping with other peaks. The expression of R_{hkl} is given by Eq. [2]^[20]:

$$R_{hkl} = \frac{1}{v^2} \left[|F_{hkl}|^2 p_{hkl} \left(\frac{1 + \cos^2 2\theta_{hkl}}{\sin^2 \theta_{hkl} \cos \theta_{hkl}} \right) \right] (e^{-2M}). \quad [2]$$

where F_{hkl} is the structure factor for diffracting plane $\{hkl\}$, p is multiplicity factor, and e^{-2M} is the Debye–Waller factor. For simplicity, Debye–Waller factor was assumed to be unity as the measurement was performed at room temperature. Atom positions of Zr and hydrogen in δ -hydride and atom positions of Zr in α -Zr are available from the published literature,^[21] which were used for structure factor F_{hkl} calculation.^[20] Table II summarizes the parameters that were used for the factor R calculation.

Hydrogen concentration (in wppm) can be calculated using the volume ratio of δ -hydride and α -Zr, as shown in Eq. [3]

$$C_H = 10^6 \frac{1.66\rho_{\delta}V_{\delta}/V_{\alpha}}{M_{\delta}\rho_{\alpha} + M_{\alpha}\rho_{\delta}V_{\delta}/V_{\alpha} + 1.66\rho_{\delta}V_{\delta}/V_{\alpha}}, \quad [3]$$

where M_{α} and M_{δ} are the atomic and molecular masses of α -Zr and δ -hydrides, respectively; ρ_{α} and ρ_{δ} are the densities of α -Zr and δ -hydride phases, respectively; and a factor of 1.66 is the atomic ratio of hydrogen to zirconium in δ -hydride. Volume fraction of hydride can be calculated from the volume ratio of δ -hydride phase and α -Zr phase using Eq. [4]. Hydrogen concentrations and hydride volume fractions for different samples were calculated, and are listed in Table III. A hydrogen concentration of 1046 wppm was observed in the CrAl-20hr. As will be shown later, both grain boundary hydride and intragranular hydride particles were observed. Hydrogen concentration calculated by the synchrotron X-ray diffraction is the overall hydrogen concentration that includes both grain boundary hydride and intragranular hydride particles. Intragranular hydride particles was observed using TEM, and the hydrogen concentration of inside grains of Zircaloy matrix will be estimated for CrAl-20hr using TEM, which are described in Section III–D.

Table II. Parameters Used for the Factor R Calculation and Integrated Intensity for α -Zr (101) Peak and δ -ZrH_{1.66} (220) Peak for CrAl-20hr

	α -Zr (101)	δ -ZrH _{1.66} (220)
Volume of Unit Cell v (\AA^3)	46.57	109.28
Structure Factor $ F _{hkl}$	54.4	110.5
Multiplicity Factor p_{hkl}	12	12
Diffraction Angle θ_{hkl}	1.367	1.996
Factor R_{hkl} (\AA^{-6})	28759.7	10116.1
Atomic Scattering Factor f_{Zr}	31.4	27.2
Atomic Scattering Factor f_H	—	0.26
Integrated Intensity I_{hkl}	148,553	3764

Table III. Volume Fractions of Hydride and Hydrogen Concentrations for Different Samples

Sample ID	Hydride Volume Fraction (Percent)	Hydrogen Concentration (wppm)
CrAl-1hr	0.18	28
CrAl-3hr	1.30	200
CrAl-5hr	2.73	422
CrAl-10hr	6.23	969
CrAl-20hr	6.70	1046

$$VF_{\delta} = \frac{V_{\delta}}{V_{\delta} + V_{\alpha}} = \frac{1}{1 + \frac{1}{V_{\delta}/V_{\alpha}}} \quad [4]$$

Crystallographic texture was not taken into account in the hydrogen concentration calculation, as Eqs. [1] and [2] are for grains with random orientations. However, justification of the hydrogen concentrations from the synchrotron XRD calculations was performed by two methods; (1) comparison of the diffraction pattern of CrAl-20hr to Zircaloy-4 with a known hydrogen concentration, (2) direct hydrogen concentration measurement by LECO combustion analysis.

The comparison is shown in Figure 4, the synchrotron diffraction patterns of the CrAl-20hr sample vs the Zircaloy-4 sample with a known hydrogen concentration of 977wppm.^[22] Both patterns were normalized to their largest peaks α -Zr(101). Equations [1] through [4] were used to calculate the hydrogen concentration in Zircaloy-4. The calculated hydrogen concentration in Zircaloy-4 was 1160 wppm. This estimation using synchrotron XRD calculation is 18.7 pct higher than the known value.

The LECO combustion analysis was performed by the NSL ANALYTICAL on the CrAl-20hr sample. This analysis incorporates gas fusion under a flow of inert Ar gas, and the hydrogen was measured by the infrared absorption and thermal conductivity. The hydrogen concentration in CrAl-20hr was measured to be 1122 ± 168 wppm. The estimation using the synchrotron XRD calculation (1046 wppm) is only 6.8 pct lower from the LECO combustion analysis results. Although the estimated hydrogen concentrations from the synchrotron

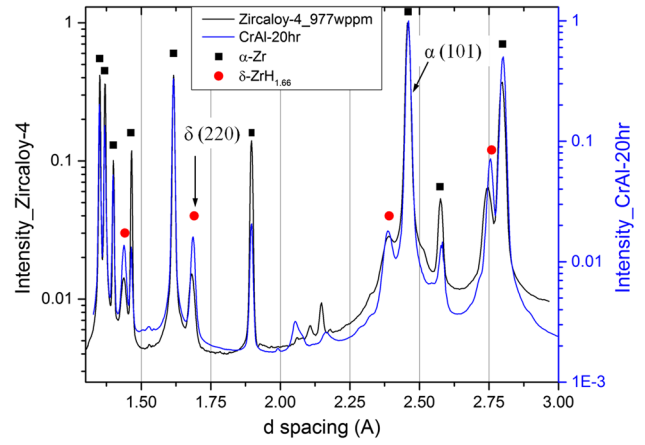


Fig. 4—Synchrotron XRD comparison of CrAl-20hr to Zircaloy-4 with 977 wppm hydrogen. The diffraction pattern of Zircaloy-4 with 977 wppm hydrogen is drawn from our previous publication.^[22]

XRD calculation show different trends to the known value of Zircaloy-4 and to the LECO combustion analysis result of Zircaloy-2, this difference could be attributed to the different texture of different materials, and thus lead to errors associated with the synchrotron XRD calculation. However, more importantly, the estimated hydrogen concentration from the synchrotron XRD peak intensity calculation is in a good agreement with the direct hydrogen measurement. Based on the justification, the calculated hydrogen concentration using Eqs. [1] through [4] is reasonable and can be used to estimate the hydrogen concentrations for different samples.

B. Synchrotron X-Ray Diffraction Analysis on Second-Phase Particles

Figure 3(b) shows the diffraction pattern range containing the (411) and (213) $Zr_2(Fe,Ni)$ peaks. These were chosen as they did not overlap with stronger reflections. Intermetallic SPPs' peaks became broader and shifted as the hydrogen concentration increased. Pseudo-Voigt peak fitting was performed on samples up to 5 hours exposure. Fitting was not reliable for 10 hours and 20 hours exposures, as peaks became too broad. Peak centroid, full width half maximum (FWHM), and integrated intensity are listed in Table IV. Both peaks became broader and exhibited lower integrated intensity as hydrogen concentration increased. This indicates that the volume fraction of crystalline $Zr_2(Fe,Ni)$ SPPs and the average particle size decreased as hydrogen concentration increased. In addition, the peak shifts suggested that the lattice parameters of $Zr_2(Fe,Ni)$ SPPs changed as the hydrogen concentration increased.

Figure 3(c) shows the diffraction patterns from strong $Zr(Fe,Cr)_2$ SPPs' peaks. In the same way as for the $Zr_2(Fe,Ni)$ peaks, fitting of the (112) $Zr(Fe,Cr)_2$ peak was performed to quantitate the integrated intensity, peaks' positions, and FWHM. $Zr(Fe,Cr)_2$ (004) peak at 2.07 Å overlays with the diffraction peaks from the coating, as labeled in Figure 3(a). The coating was consumed under this exposure condition, and its

Table IV. Peak Center, FWHM, and Integrated Area Intensities for SPPs, $Zr_2(Fe,Ni)$ (411), and $Zr_2(Fe,Ni)$ (213) Peaks Shown in Fig. 3(b), and $Zr(Fe,Cr)_2$ (112) Peak in Fig. 3(c)

Sample	$Zr_2(Fe,Ni)$ (411) peak			$Zr_2(Fe,Ni)$ (213) peak			$Zr(Fe,Cr)_2$ (112) peak		
	Center Position[Å]	FWHM [Å]	Integrated Intensity	Center Position[Å]	FWHM [Å]	Integrated Intensity	Center Position[Å]	FWHM [Å]	Integrated Intensity
CrAl-0hr	1.51077	0.00633	28.9	1.52550	0.00691	47.1	2.15654	0.01068	96.6
CrAl-1hr	1.51165	0.00645	25.1	1.52549	0.00709	45.1	2.15697	0.01100	95.5
CrAl-3hr	1.51219	0.00751	25.0	1.52556	0.00779	42.1	2.15645	0.01145	95.5
CrAl-5hr	1.51269	0.00875	24.6	1.52565	0.00814	40.5	2.15613	0.01208	96.4

diffraction intensity is expected to change as a function of exposure time. Therefore, only the strongest (112) peak of $Zr(Fe,Cr)_2$ was selected for fitting, which does not overlay with other peaks. The results are listed in Table IV. Unlike $Zr_2(Fe,Ni)$, the integrated peak intensity of $Zr(Fe,Cr)_2$ did not change noticeably. This suggests that hydrogen has a larger effect on the stability of $Zr_2(Fe,Ni)$ compared to $Zr(Fe,Cr)_2$ up to the hydrogen concentration of 422 wppm. However, at higher hydrogen concentration, approximately 1000 wppm, diffraction peaks from both SPPs become much broader.

C. Size Distribution of Second-Phase Particles

Cross-sectional SEM was applied to characterize the microstructure and to determine SPPs' size distribution and volume fraction. Cross-sectional SEM images of CrAl-0hr, CrAl-5hr, and CrAl-20hr are shown in Figure 5. The SEM images were taken randomly at the center of the cross section of Zircaloy sample far from the sample edges. Figure 5(a) shows the microstructure of CrAl-0hr matrix, which is the same as that of the as-received Zircaloy-2. Grain size of the Zircaloy-2 ranged from 10 to 20 μm . Intermetallic SPPs appear as black dots in the low magnification image in Figure 5(a). The hydride phase was preferentially attacked by the chemical etching and appears as line-like features in Figure 5(c). Large hydride particles are observed, which accumulate at grain boundaries at higher hydrogen concentration in CrAl-20hr, as shown in Figure 5(e). Intragranular hydride particles were also observed. However, the sizes of intragranular hydride particles were small and not evident in SEM images. Although hydrogen was generated and absorbed by the steam oxidation on the sample edges, the hydride distribution was uniform throughout the bulk due to the fast diffusivity of hydrogen in Zircaloy.^[23]

The SPPs' size distribution was determined based on the cross-sectional images at the 10,000 times magnification as shown in Figures 5(b), (d) and (f). Approximately 200 particles were examined in each sample, and the total imaging area for the size analysis is over 900 μm^2 up to 1600 μm^2 for each sample. Table V includes the total imaging area for each sample. The final cross-sectional polishing step was the use of 50 nm silica solution, and particles below 50 nm were not characterized. The two types of SPPs were not differentiated in the size distribution study due to the difficulty

in performing chemical analysis on all particles, and the lifting-out of some of the particles during the mechanical polishing.

Figure 6 shows the normalized size distribution of intermetallic SPPs of CrAl-0hr, CrAl-5hr, and CrAl-20hr. Particles with a diameter of 150-200 nm have the largest frequency, with particles over 650 nm occasionally observed. Similar SPPs' size distributions in Zircaloy-2 have been reported previously.^[2] As hydrogen concentration increased, the frequencies of larger particles (> 250 nm) decreased, while the frequencies of 100 to 200 nm particle sizes increased. This suggests that intermetallic SPPs dissolved at high hydrogen concentrations. In addition, the observation of particle size reduction in higher hydrogen concentration could lead to broader diffraction peaks of SPPs, as shown in Figure 3(b).

To estimate the volume fraction of intermetallic SPPs, particles were assumed to be spherical, with a radius equal to the measured radius. The volume fraction of intermetallic SPPs was calculated using SPPs spherical volumes, and the observation area times the depth, which is selected as the average diameter of SPPs (approximately 200 nm). The depth was selected because only particles within this depth range were exposed and could be observed. Table V shows the number of particles examined and the calculated volume fractions and the areal number densities of intermetallic SPPs. The SPP volume fraction decreases as the hydrogen concentration increases, with the volume fraction at 1046 wppm hydrogen equal to 0.4 pct, compared to 1.7 pct for the as-received material. The reductions of the volume fractions of intermetallic SPPs are in agreement with the decreasing integrated intensity of SPPs in synchrotron XRD in Figure 3. The areal number densities of SPPs were also quantified. The original areal number density of SPPs in unexposed Zircaloy-2 was 21.06×10^4 particle/ mm^2 ; this dropped to two-thirds of the original density at 1046 wppm hydrogen concentration. Errors associated with the size distribution and the estimated volume fraction using this method are presented in Section IV-B.

D. Microstructures of Hydride and Intermetallic SPPs

Figure 7(a) shows the microstructures of intragranular hydride particles and intermetallic SPPs at the center of the CrAl-20hr sample. Hydride particles with needle-like morphology were observed inside grains. Most

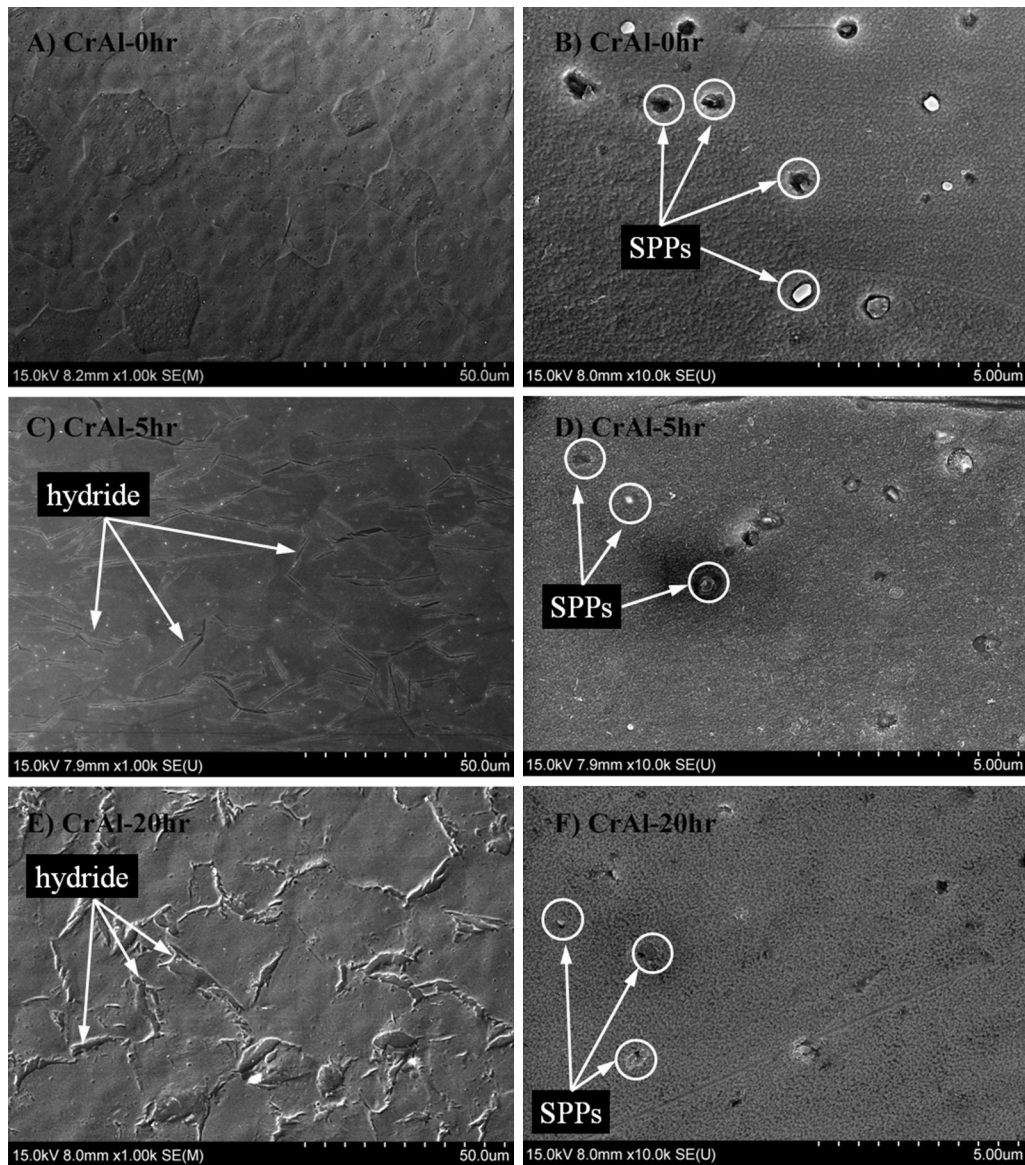


Fig. 5—Cross-sectional images of (a, b) CrAl-0hr, (c, d) CrAl-5hr, and (e, f) CrAl-20hr. Lower magnification images (a, c, e) show grain structure and hydride distribution for CrAl-5hr and CrAl-20hr. High-magnification images at 10000 times magnification (b, d, f) are used for particle size distribution quantification. Intermetallic SPPs are circled.

intragranular hydride particles were 10 to 35 nm wide and 50 to 300 nm long, and aligned. Diffraction patterns of the intragranular hydride particles and the Zr matrix were performed and shown in Figure 7(c). The diffraction patterns were taken on the α -Zr $[2\bar{1}\bar{1}0]$ zone axis. The δ -hydride (Fm3m) was identified based on the TEM diffraction pattern, which is in agreement with the synchrotron XRD (Figure 3(a)). The δ -hydride has the $(0002)_{\alpha} \parallel (11\bar{1})_{\delta}$ and $[2\bar{1}\bar{1}0]_{\alpha} \parallel [011]_{\delta}$ orientation relationship with the Zr matrix, which was also observed by others.^[24,25] Due to the close vicinity of α -Zr (0002) and δ -hydride (111) diffraction, and the strong diffraction intensity of α -Zr matrix, the diffraction of δ -hydride (111) was not clearly observed in the pattern in Figure 7(c). Two intermetallic SPPs are highlighted in Figure 7(b), and they are identified as $Zr_2(Fe,Ni)$ based on the EDS measurement. The sizes of these two

intermetallic SPPs are 130 and 150 nm, respectively, which are the dominant sizes of intermetallic SPPs, as shown in Figure 6. These intermetallic SPPs were surrounded by a dense distribution of intragranular hydride particles. Although hydride particles are in proximity to the $Zr_2(Fe,Ni)$ SPP, no orientation relationship was observed between the hydride particles and the second-phase particles.

Both grain boundary hydride (Figure 3) and intragranular hydride particles (Figure 7) are observed. The intragranular hydride particles are too small for the SEM analysis. Therefore, TEM was applied to study the volume fraction of intragranular hydride particles and the intragranular hydrogen concentration. The volume of intragranular hydride was estimated using the TEM image in Figure 7(a), assuming tetragonal shape of intragranular hydride particles and the TEM sample

Table V. Volume Fractions and Areal Densities of the Intermetallic SPPs

	CrAl-0hr	CrAl-5hr	CrAl-20hr
Total Analyzed Particles	261	182	205
Total Image Area (μm^2)	1240	901	1577
Hydrogen Concentration (wppm)	0	422	1046
Volume Fraction (Percent)	1.7 pct	1.4 pct	0.4 pct
Areal Number Density ($\times 10^4/\text{mm}^2$)	21.06	20.19	15.97

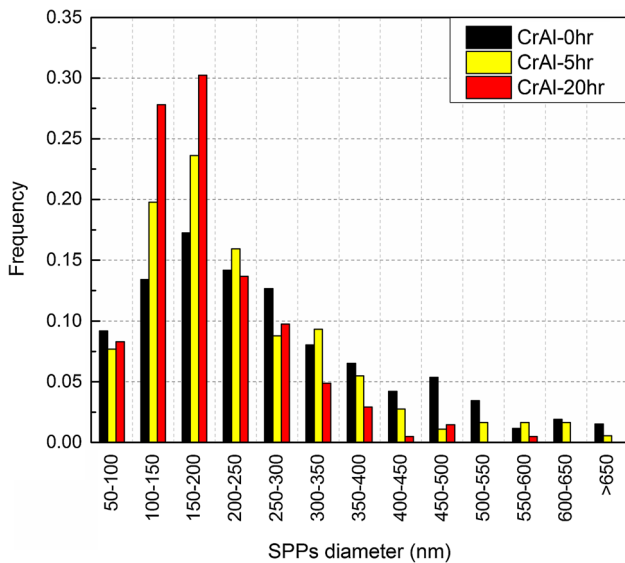


Fig. 6—Normalized size distribution of SPPs based on the SEM images. Dominant particle sizes are within 100 to 200 nm range. At higher hydrogen concentration, frequencies of large SPPs decreased, while the frequencies of 100–200 nm particle sizes increased.

thickness as 150 nm. The volume fraction of intragranular hydride was calculated as 2.2 pct, which corresponds to the hydrogen concentration of 370 wppm. The lower intragranular hydrogen concentration than the overall hydrogen concentration indicates the preferential hydriding at grain boundaries, which was also observed in other studies.^[26]

The chemical composition line-profile across one of the $\text{Zr}_2(\text{Fe},\text{Ni})$ particles is provided in Figure 7(d), as labeled in the TEM image in Figure 7(b). The line-scan measurement was attempted in order to characterize the concentration gradient within the particle. The composition profiles of Zr, Fe, and Ni were measured, as shown in Figure 7(d). The region between the two dashed lines represents the $\text{Zr}_2(\text{Fe},\text{Ni})$ SPP, and these two dashed lines are based on the size of the particle in Figure 7(a). At first glance, there appears to be concentration gradients within the particle. However, these concentration gradients are attributed to the SPPs' volume difference. The SPP has a spherical shape, and its diameter is close to the thickness of the TEM sample. The measured composition has the contributions from both the $\text{Zr}_2(\text{Fe},\text{Ni})$ SPP and the Zr matrix. Therefore, the composition gradient could be simply due to the volume difference of SPPs due to its spherical shape. And the measurement for the composition gradient within the particle is difficult in this case. In the matrix

close to the interface of the SPP, there are no measurable concentrations of Fe and Ni, as shown in Figure 7(d). However, if there are Fe and Ni solutions in the Zircaloy-2 matrix, they have lower concentrations than the measurement limit.

IV. DISCUSSION

A. Factors Contributing to Second-Phase Particles Dissolution

The dissolution of SPPs under the high-temperature steam environment has not been reported previously, and the mechanism that leads to the SPPs' dissolution is not clear. Unlike Zirconium Excel alloy,^[27] Zircaloy-2 only contains α -Zr phase at the tested temperature (700 °C). The dissolution temperatures of different intermetallic SPPs in different Zr-based alloys were studied,^[28] and the dissolution of $\text{Zr}(\text{Fe},\text{Cr})_2$ SPPs in Zircaloy-4 does not occur during the high-temperature annealing until the temperature is close to α -Zr/ β -Zr transition temperature (above 800 °C).^[28] Therefore, the dissolution of SPPs in Zircaloy-2 at 700 °C indicates the effect of the hydrogen presence to the dissolution of intermetallic SPPs in this system. In this section, we present a possible mechanism that could lead to the SPPs' dissolution, and other factors that could contribute to the dissolution.

Hydrogen concentration is correlated with the volume fraction of intermetallic SPPs, and the volume fraction of intermetallic SPPs decreased as hydrogen concentration increased (Table V). Although the hydrogen solubilities in the intermetallic SPPs in Zircaloy have not been measured to our best knowledge, binary intermetallic phases, such as Zr_2Ni , Zr_2Fe , and ZrCr_2 , are known to accommodate hydrogen at interstitial sites.^[29–31] Hydrogen-containing intermetallic phases form as Zr_2NiH_x , Zr_2FeH_x , and ZrCr_2H_x , where x can be as high as 5.1 in the formula.^[29–31] These hydrogen-containing intermetallic phases maintain the same crystal lattice structures as the intermetallic phases, and the lattice parameters increase with the hydrogen solution concentration.^[31]

Ternary intermetallic phases $\text{Zr}_2(\text{Fe},\text{Ni})$ and $\text{Zr}(\text{Fe},\text{Cr})_2$ have same crystallographic structures as Zr_2Ni , Zr_2Fe (space group as $I4/mcm$) and ZrCr_2 (space group as $p63/mmc$). Therefore, it is reasonable to assume that the ternary intermetallic phases $\text{Zr}_2(\text{Fe},\text{Ni})$ and $\text{Zr}(\text{Fe},\text{Cr})_2$ would also accommodate hydrogen solution at the interstitial sites,^[32] and the hydrogen solution generates large strain in SPPs.^[33] In fact, the

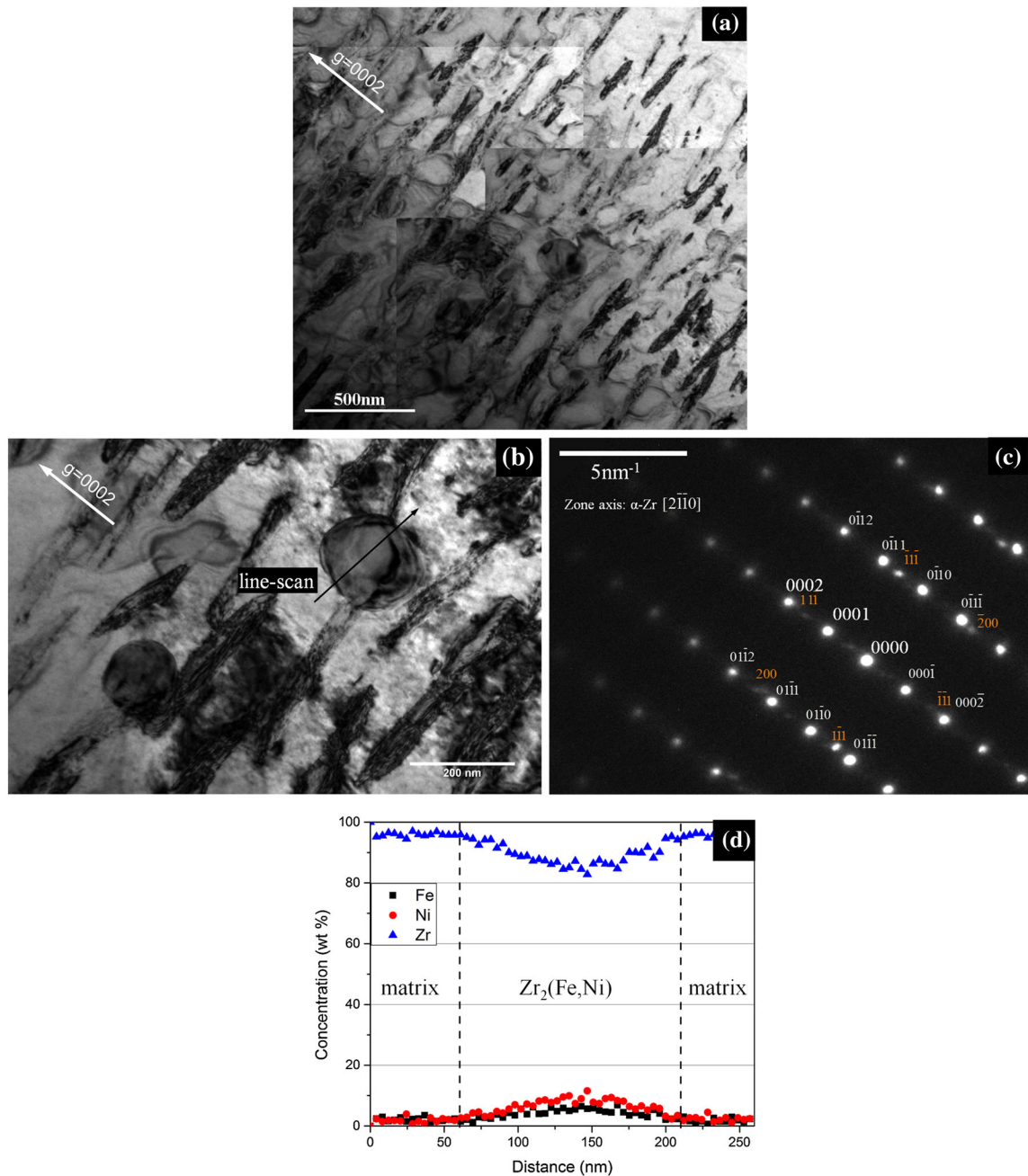


Fig. 7—Microstructures of intragranular hydride and intermetallic SPPs at the center of the CrAl-20hr sample. (a) TEM image of the Zircaloy substrate, where needle-like hydrides are oriented along the basal plane. (b) A dense distribution of intragranular hydride particles near two intermetallic SPPs $Zr_2(Fe,Ni)$. (c) Diffraction patterns from the α -Zr and intragranular δ -hydride, taken at the α -Zr $[2\bar{1}10]$ zone axis. Diffractions from α -Zr are labeled in white, and δ -hydride in orange. The δ -hydride has the $(0002)_z \parallel (1\bar{1}\bar{1})_\delta$ and $[2\bar{1}\bar{1}0]_z \parallel [011]_\delta$ orientation relationship with the Zr matrix. (d) Composition profiles of Zr, Fe, and Ni across the $Zr_2(Fe,Ni)$ SPP. The location of the line-scan is labeled in (b). Composition gradient within $Zr_2(Fe,Ni)$ SPP is attributed to the volume difference of SPPs within the measured volume.

shifts of peak center of $Zr(Fe,Ni)_2$ to higher d-spacing might indicate the presence of hydrogen solution in intermetallic SPPs (Figure 3(b)).

The preferred interstitial sites for hydrogen solution depend on the hydrogen concentration,^[34] and it is found that non-uniformed distribution of hydrogen accommodation in the available sites could contribute to the peak broadening in the X-ray diffraction.^[35] The peak broadening of SPPs was also observed from the

synchrotron X-ray diffraction in this case (Figure 3), which could also have the effect from the nonuniform distribution of hydrogen accommodation in SPPs in Zircaloy-2.

In addition to the strain accompanying with the hydrogen solution in SPPs, the hydride formation in Zircaloy matrix leads to significant strain due to the volumetric dilatation of hydride.^[24,36,37] A dense intragranular hydride particle distribution was observed

around the intermetallic SPPs, as shown in TEM image in Figure 7. The resulting strain energy from the hydrogen solution in the SPPs and the dense distribution of intragranular hydride particles could lead to dissolution in high-temperature environment. Although the dissolution of either type of SPPs in Zircaloy-2 has not been reported (C16 Laves phase $Zr_2(Fe,Ni)$ or C15 Laves phase $Zr(Fe,Cr)_2$), hydrogen-induced instability of many other Laves phases has been observed.^[30,38,39] In those publications, it was determined that hydrogen absorption in Laves phase AB_2 could lead to decomposition of the Laves phase into hydride and other intermetallic phases, depending on the temperature and hydrogen pressure.^[30,38,39] However, transformation of SPPs to other intermetallic phases was not observed in this case.

In addition, hydrogen solution in binary Zirconium intermetallic SPPs was studied using DFT.^[26] It was suggested that hydrogen is preferentially attracted to $Zr_2(Fe,Ni)$ over $Zr(Fe,Cr)_2$. This is in an agreement with the observation that $Zr_2(Fe,Ni)$ SPPs started to dissolve before $Zr(Fe,Cr)_2$ from the synchrotron XRD (see Figure 3).

The chromium-aluminum coating on the surface of the Zircaloy coupon and Zr oxide formation at the edges did not contribute to the SPPs' dissolution in this system. We have characterized oxidation of this system previously.^[16] Interaction of coating and substrate was limited to the top 3 μm of the surface, as measured by STEM, and Zircaloy oxidation at the edges leads to 85- μm -thick oxide formation in 10 hours and 155- μm -thick oxide formation in 20 hours.^[16] The SEM analysis of the SPPs was performed on the center of the cross-sectional Zircaloy matrix, which was 500 μm away from the coating and at least 2 mm away from the oxide on the edges. Also the transmission synchrotron diffraction probed the full thickness of the sample, minimizing the effects of the near coating/matrix regions. Therefore, we believed the coating and Zr oxide formation did not contribute to the SPPs' dissolution.

B. Error Analysis on Particle Volume Estimation

We address the error in the volume fraction estimation of intermetallic SPPs and potential error using 2D cross-sectional SEM images in this section. First, particles below 50 nm were not examined, so the total SPPs' volume did not include small particles. However, from the SPPs' size distribution histogram in Figure 6, small particles (< 50 nm) are presumed to have a low frequency,^[2] so the volume contribution from these small particles is expected to be small.

The second error source is due to 3D particle size examination from 2D images. Particles were assumed spherical, but the measured diameters on 2D images were not necessarily the diameters on great circles of spherical particles. The measured diameters could be smaller than the actual particle diameters if they were only partially exposed. However, this error is systematic for all measured samples. Therefore, the hydrogen concentration correlation to the volume fraction of

SPPs is still valid, but the volume fraction could be underestimated. In addition, all SPPs were not necessarily spherical. Particles with the elliptical cross sections were observed. In this case, the diameter was selected to be 45 deg between the minor and major axes. This error is not significant for the volume calculation.

Lastly, SPPs' clusters have been observed previously.^[16,40] However, SEM analysis at 10,000 times magnification does not necessarily have the ability to detect the particle clusters if the particles sizes are small. In this study, one cluster is considered a particle, leading to error associated with the particle size distribution, but not necessarily volume fraction. However, SPPs' clusters are not frequently observed, and we believed that this error was not significant, and the size distribution and volume fraction are considered reasonable.

V. CONCLUSION

Chromium-Aluminum-coated Zircaloy-2 coupons were oxidized in 700 °C steam environment for up to 20 hours. Hydrogen was generated during this exposure to the steam oxidation of uncoated Zr. δ -hydrides formed in the Zircaloy matrix. Both intergranular and intragranular hydride particles were observed. Hydrogen concentration was estimated from the synchrotron XRD, and it increased with longer exposure times. Although the calculation did not take crystalline texture into account, the estimated hydrogen concentration is reasonable compared with the LECO combustion hydrogen measurement and to Zircaloy-4 with the known hydrogen concentration.

Volume fractions of the intermetallic second-phase particles were estimated based on the SEM analysis of the size distribution of intermetallic SPPs. Despite the errors associated with the 2D SEM analysis method, the trend shows that the frequencies of larger particles decreased and the volume fraction of the intermetallic SPPs decreased at longer exposure time. This result was in an agreement with the synchrotron XRD analysis, where the diffraction peaks of intermetallic SPPs became broader and the integrated peak intensity of intermetallic SPPs decreased at longer exposure time.

These observations suggest hydrogen-induced dissolution of intermetallic SPPs in Zircaloy during the high-temperature steam oxidation. Although the mechanism of SPPs' dissolution was not fully understood, others have observed that hydrogen induced instability of many other Laves phases systems, which have same structures as intermetallic SPPs in Zircaloy-2.^[30,38,39]

ACKNOWLEDGMENTS

This study was supported by the US Department of Energy Nuclear Energy University Programs Integrated Research Project under Contract Number IRP-12-4728; supported by the University of Illinois Campus Research Board under Award Number RB17006; and

supported by Laboratory Directed Research and Development (LDRD) Program (Project No. 13-027) at BNL. The microanalysis was performed in the Frederick Seitz Materials Research Laboratory Central Facilities, University of Illinois, which are partially supported by the US Department of Energy under Grants DE-FG02-07ER46453 and DE-FG02-07ER46471. This research used resources of the Advanced Photon Source, a U.S. Department of Energy (DOE) Office of Science User Facility operated for the DOE Office of Science by Argonne National Laboratory under Contract No. DE-AC02-06CH11357. The authors are grateful to Richard Spence (APS) for his help with synchrotron XRD measurement.

REFERENCES

- G.P. Sabol: *J. ASTM Int.*, 2005, vol. 2, pp. 3–24.
- R.M. Kruger, R.B. Adamson, and S.S. Brenner: *J. Nucl. Mater.*, 1992, vol. 189, pp. 193–200.
- S.C. Lumley, S.T. Murphy, P.A. Burr, R.W. Grimes, P.R. Chard-Tuckey, and M.R. Wenman: *J. Nucl. Mater.*, 2013, vol. 437, pp. 122–29.
- X. Meng and D.O. Northwood: *J. Nucl. Mater.*, 1989, vol. 168, pp. 125–36.
- P. Rudling, K. L. Vannesjö, G. Vesterlund, and A. R. Massih: *Zirconium in the Nuclear Industry: Seventh International Symposium, ASTM STP 939*, 1987, pp. 292–306.
- Y. Hatano, K. Isobe, R. Hitaka, and M. Sugisaki: *J. Nucl. Sci. Technol.*, 1996, vol. 33, pp. 944–49.
- J. Wang, H. Fan, J. Xiong, H. Liu, Z. Miao, S. Ying, and G. Yang: *Nucl. Eng. Des.*, 2011, vol. 241, pp. 471–75.
- M. Yao, J. Wang, J. Peng, B. Zhou, and Q. Li: *J. ASTM Int.*, 2011, vol. 8, pp. 466–95.
- P. Tägtstrom, M. Limbäck, M. Dahlbäck, T. Andersson, and H. Pettersson: *Zirconium in the Nuclear Industry: Thirteenth International Symposium, ASTM STP 1423*, 2002, pp. 96–118.
- Y. Hatano, M. Sugisaki, K. Kitano, and M. Hayashi: *Zirconium in the Nuclear Industry: Twelfth International Symposium, ASTM STP 1354*, 2000, pp. 901–17.
- D.F. Taylor: *J. Nucl. Mater.*, 1991, vol. 184, pp. 65–77.
- B.C. Cheng, R.M. Kruger, and R.B. Adamson: *Zirconium in the Nuclear Industry: Tenth International Symposium, ASTM STP 1245*, 1994, pp. 400–18.
- M. Griffiths, R.W. Gilbert, and G.J.C. Carpenter: *J. Nucl. Mater.*, 1987, vol. 150, pp. 53–66.
- A.T. Motta and C. Lemaignan: *J. Nucl. Mater.*, 1992, vol. 195, pp. 227–85.
- P. Vizcaino, A. Flores, P. Bozzano, A. Banchik, R. Versaci, and R. Rios: *J. ASTM Int.*, 2011, vol. 8, pp. 754–83.
- W. Zhong, P.A. Mouche, and B.J. Heuser: *J. Nucl. Mater.*, 2018, vol. 498, pp. 137–48.
- W. Zhong, P.A. Mouche, X. Han, B.J. Heuser, K.K. Mandapaka, and G.S. Was: *J. Nucl. Mater.*, 2016, vol. 470, pp. 327–38.
- M.M. Strehle, B.J. Heuser, M.S. Elbakhshwan, X. Han, D.J. Gennardo, H.K. Pappas, and H. Ju: *Thin Solid Films*, 2012, vol. 520, pp. 5616–26.
- R.S. Daum, Y.S. Chu, and A.T. Motta: *J. Nucl. Mater.*, 2009, vol. 392, pp. 453–63.
- B.D. Cullity: *Elements of X-ray Diffraction*, Addison-Wesley Publishing Co., Inc., Melbourne, 1956, pp. 104–37.
- S.S. Sidhu, N.S. Satya Murthy, F.P. Campos, and D.D. Zauberis: No. ANL-FGF-332; UAC-6209. Argonne National Lab., 1963, pp. 87–98.
- J.L. Lin, X. Han, B.J. Heuser, and J.D. Almer: *J. Nucl. Mater.*, 2016, vol. 471, pp. 299–307.
- J.J. Kearns: *J. Nucl. Mater.*, 1972, vol. 43, pp. 330–38.
- A.T.W. Barrow, A. Korinek, and M.R. Daymond: *J. Nucl. Mater.*, 2013, vol. 432, pp. 366–70.
- K. Une, K. Nogita, S. Ishimoto, and K. Ogata: *J. Nucl. Sci. Technol.*, 2004, vol. 41, pp. 731–40.
- K.M. Krishna, A. Sain, I. Samajdar, G.K. Dey, D. Srivastava, S. Neogy, R. Tewari, and S. Banerjee: *Acta Mater.*, 2006, vol. 54, pp. 4665–75.
- C. Cochrane and M.R. Daymond: *Metall. Mater. Trans. A*, 2018, vol. 49A, pp. 3468–85.
- C. Toffolon-Masclat, T. Guilbert, and J.C. Brachet: *J. Nucl. Mater.*, 2008, vol. 372, pp. 367–78.
- M.P. Pitt, L.K.W. Pitt, H. Fjellvåg, and B.C. Hauback: *J. Alloys Compd.*, 2011, vol. 509, pp. 5515–24.
- M.H. Sørby, H. Fjellvåg, and B.C. Hauback: *J. Alloys Compd.*, 2005, vol. 394, pp. 107–15.
- F. Aubertin and S.J. Campbell: *Hyperfine Interact.*, 1990, vol. 54, pp. 767–73.
- P.A. Burr, S.T. Murphy, S.C. Lumley, M.R. Wenman, and R.W. Grimes: *Corros. Sci.*, 2013, vol. 69, pp. 1–4.
- H.W. Li, K. Ishikawa, and K. Aoki: *J. Alloys Compd.*, 2005, vol. 88, pp. 49–58.
- P. Raj, P. Suryanarayana, A. Sathyamoorthy, K. Shashikala, and R.M. Iyer: *J. Alloys Compd.*, 1992, vol. 178, pp. 393–401.
- J.M. Filho, A.W. Carbonari, W. Pendl, Jr, J.I. Moura, and R.N. Saxena: *J. Alloys Compd.*, 1995, vol. 224, pp. 60–65.
- J.L. Lin, W. Zhong, H.Z. Bilheux, and B.J. Heuser: *J. Nucl. Mater.*, 2017, vol. 496, pp. 129–39.
- G.J.C. Carpenter: *J. Nucl. Mater.*, 1973, vol. 48, pp. 264–66.
- K. Aoki, X.G. Li, and T. Masumoto: *Acta Metall. et Mater.*, 1992, vol. 40, pp. 1717–26.
- K. Ishikawa, N. Ogasawara, and K. Aoki: *Philos. Mag. Lett.*, 2004, vol. 84, pp. 207–14.
- P. Chemelle, D.B. Knorr, J.B. Van Der Sande, and R.M. Pelloux: *J. Nucl. Mater.*, 1983, vol. 113, pp. 58–64.